9. Reichlin, R. *et al.* Evidence for the insulator-metal transition in xenon from optical, x-ray and band structure studies to 170 GPa. *Phys. Rev. Lett.* **62,** 669–672 (1989).
10. Goettel, K. A., Eggert, J. H. & Silvera, I. F. Optical evidence for the metallization of xenon at 132 (5) GPa. *Phys. Rev. Lett.* **62,** 665–672 (1989).
11. Luo, H., Desgreniers, S., Vohra, Y. K. & Ruoff, A. L. High pressure optical studies on sulfur to 121 GPa: optical evidence for metallization. *Phys. Rev. Lett.* **67,** 2998–3001 (1991).
12. Desgreniers, S., Vohra, Y. K. & Ruoff, A. L. Optical response of very high density solid oxygen to 132 GPa. *J. Phys. Chem.* **94,** 1117–1122 (1990).
13. Jayaraman, A. Diamond anvil cell and high pressure physical investigations. *Rev. Mod. Phys.* **55,** 65–108 (1983).
14. Kawai, N., Togaya, M. & Mishima, O. A study of the metallic hydrogen. *Proc. Japan Acad.* **51,** 630–633 (1975).
15. Vereshchagin, L. F., Yakovlev, E. N. & Timofeev, Yu A. Possibility of transition of hydrogen into the metallic state. *JETP Lett.* **21,** 85–86 (1975).
16. Hawke, P. S. *et al.* Observation of electrical conductivity of isotropically compressed hydrogen at megabar pressures. *Phys. Rev. Lett.* **4,** 994–997 (1978).
17. Burgess, T. G. & Hawke, R. S. *Metallic Hydrogen Research* 1–26 (Rep. UCID-17977, Lawrence Livermore Lab., CA, 1978).
18. Mao, H. K. & Hemley, R. J. Optical studies of hydrogen above 200 gigapascals: evidence for metallization by band overlap. *Science* **244,** 1462–1465 (1989).
19. Mao, H. K., Hemley, R. J. & Hanfland, N. Infrared reflectance measurements of the insulator-metal transition in solid hydrogen. *Phys. Rev. Lett.* **65,** 484–487 (1990).
20. Hanfland, M., Hemley, R. J. & Mao, H. K. Optical absorption measurements of hydrogen at megabar pressures. *Phys. Rev. B* **43,** 8767–8770 (1991).
21. Eggert, J. H., Goettel, K. A. & Silvera, I. F. High-pressure dielectric catastrophe and the possibility that the hydrogen A-phase is metallic. *Europhys. Lett.* **11,** 775–781 (1980).
22. Ashcroft, N. W. Dense hydrogen: the reluctant alkali. *Phys. World* **8(7),** 43–47 1995).
23. Weir, S. T., Mitchell, A. C. & Nellis, W. J. Metallization and electrical conductivity of hydrogen in Jupiter. *Phys. Rev. Lett.* **76,** 1860–1863 (1996).
24. Ruoff, A. L., Xia, H., Luo, H. & Vohra, Y. K. Miniaturization techniques for obtaining static pressures comparable to the pressure at the center of the earth: x-ray diffraction at 416 GPa. *Rev. Sci. Instrum.* **61,** 3830–3833 (1990).
25. Ruoff, A. L., Xia, H. & Xia, Q. The effect of a tapered aperture on x-ray diffraction from a sample with a pressure gradient: studies on three samples with a maximum pressure of 560 GPa. *Rev. Sci. Instrum.* **63,** 4342–4348 (1992).
26. Ruoff, A. L. in *High Pressure Science and Technology (Proc. AIRAPT XV and EHRPG 33 Conf.)* (ed. Trzeciakowski, W.) 511 (World Scientific, Warsaw, 1996).
27. Birch, J. F. Finite strain isotherm and velocities for single crystal and polycrystalline NaCl at high pressures and 300 °K. *J. Geophys. Res.* **83,** 1257–1269 (1978).
28. McQueen, R. G., Marsh, S. P., Taylor, J. W., Fritz, J. N. & Carter, W. J. in *High Velocity Impact Phenomena* (ed. Kinslow, R.) 293–417 (Academic, New York, 1970).
29. Carter, W. J., Marsh, S. P., Fritz, J. N. & McQueen, R. J. *Accurate Characterization of the High-Pressure Environment* (ed. Lloyd, E. C.) 147–158 (Spec. Publ. 326, Natl. Bureau of Standards, Washington DC, 1971).
30. Hixson, R. S., Boneness, D. A. & Shaner, J. W. Acoustic velocities and phase transitions in molybdenum under strong shock compression. *Phys. Rev. Lett.* **62,** 637–640 (1989).
31. Christensen, N. E., Ruoff, A. L. & Rodriguez, C. O. Pressure strengthening: a way to multimegabar pressures. *Phys. Rev. B* **52,** 9121–9124 (1993).
32. Ruoff, A. L., Luo, H., Xia, H. & Vohra, Y. K. The effect of nonhydrostaticity on measuring the pressures in metals by energy dispersive x-ray diffraction. *High Press. Res.* **6,** 183–186 (1991).
33. Ruoff, A. L. Penultimate static pressure containment consideration and possible applications to metallic hydrogen preparation. *Adv. Cryogen. Eng.* **18,** 435–440 (1973).
34. Hemley, R. J. *et al.* X-ray imaging of stress and strain of diamond, iron, and tungsten at megabar pressures. *Science* **276,** 1242–1245 (1997).
35. Ruoff, A. L., Luo, H. & Vohra, Y. K. The closing diamond anvil optical window in multimegabar research. *J. Appl. Phys.* **69,** 6413–6416 (1991).
36. Kelly, A. *Strong Solids* 26 (Oxford Univ. Press, New York, 1996).
37. Stevenson, D. J. & Ashcroft, N. W. Conduction in fully ionized liquid metals. *Phys. Rev. A* **9,** 782–789 (1974).

Acknowledgements. We acknowledge discussions with N. W. Ashcroft, B. Baranowski and R. M. Martin and thank the CHESS staff for their help. We also acknowledge the role played by B. W. Batterman in creating CHESS. This work was supported by the US NSF and, several years ago in the early stages of this project, by the Cornell Materials Science Center via support by the US NSF.

Correspondence and requests for materials should be addressed to A.L.R. (e-mail: ruoff@msc.cornell.edu).

Room-temperature transistor based on a single carbon nanotube

Sander J. Tans, Alwin R. M. Verschueren & Cees Dekker

Department of Applied Physics and DIMES, Delft University of Technology, Lorentzweg 1, 2628 CJ Delft, The Netherlands

The use of individual molecules as functional electronic devices was first proposed in the 1970s (ref. 1). Since then, molecular electronics[2,3] has attracted much interest, particularly because it could lead to conceptually new miniaturization strategies in the electronics and computer industry. The realization of single-molecule devices has remained challenging, largely owing to difficulties in achieving electrical contact to individual molecules. Recent advances in nanotechnology, however, have resulted in electrical measurements on single molecules[4–7]. Here we report the fabrication of a field-effect transistor—a three-terminal switching device—that consists of one semiconducting[8–10] single-wall carbon nanotube[11,12] connected to two metal electrodes. By applying a voltage to a gate electrode, the nanotube can be switched from a conducting to an insulating state. We have previously reported[5] similar behaviour for a metallic single-wall carbon nanotube operated at extremely low temperatures. The present device, in contrast, operates at room temperature, thereby meeting an important requirement for potential practical applications. Electrical measurements on the nanotube transistor indicate that its operation characteristics can be qualitatively described by the semiclassical band-bending models currently used for traditional semiconductor devices. The fabrication of the three-terminal switching device at the level of a single molecule represents an important step towards molecular electronics.

The samples presented in this study are fabricated as described elsewhere[5,13]. Figure 1a shows an atomic force microscopy (AFM) image of a single nanotube contacting three Pt electrodes (1, 2 and 3). The semiconducting Si substrate, covered with a 300-nm layer of thermally grown SiO_2, was used as a back-gate (Fig. 1b). In our electrical transport studies on single-wall nanotubes, we have measured many individual tubes (in excess of 20) and find two types of behaviour at room temperature. The metallic variety of tubes reported previously have linear current–voltage curves (I–V_{bias}) and show no dependence on the gate voltage (V_{gate}). Here we present two-probe and three-probe measurements on the second type of sample.

Figure 2 displays I–V_{bias} curves for the sample in Fig. 1a. At $V_{gate} = 0$, a small nonlinearity seems to be present in the I–V_{bias} curve. When V_{gate} is increased to positive values, a pronounced gap-like nonlinearity develops around $V_{bias} = 0$. The curves seem to exhibit a power-law behaviour (solid lines), that is $I \propto (V_{bias})^{\alpha}$, with α between 1 and 12. Upon application of a negative V_{gate}, the I–V_{bias} curve becomes linear with a resistance that saturates around 1 MΩ. This is the same resistance that we find for the metallic tubes in a similar layout. For the major part this resistance is due to the contact resistance between the tube and the electrodes[14]. We thus obtain a controllable semiconductor-to-metal transition in a one-dimensional system. The nonlinearity at room temperature and the asymmetric dependence of the conductance on the gate voltage polarity indicate that the nanotube of this sample is semiconducting. In the inset of Fig. 2, the conductance of the device at $V_{bias} = 0$ is plotted against V_{gate}. This shows that the conductance can be strongly modulated, by about six orders of magnitude on a change of 10 V in V_{gate}. Measurements on the electrode pair 2–3 gave similar results. This sample (Fig. 1a) is one of five samples that showed a similar behaviour. In the other samples, noise due to two-level fluctuators was often larger, especially at large applied voltages. For some samples, the I–V_{bias} curves were asymmetric around $V_{bias} = 0$. Although some drift occurred along the V_{gate} axis, the transport characteristics of the sample presented here were reproducible over a period of months.

In the energy diagrams of Fig. 1c and 1d we attempt to model the electronic structure and functioning of the TUBEFET (single carbon nanotube field-effect transistor) device. The charge carriers flow through the part of the tube that is on top of the source (A), on the SiO_2 surface (B), and on the drain electrode (C) (see also Fig. 1b). Semiconducting tubes with a 1.4 nm diameter have a bandgap of ~0.6 eV (refs 15–17). As for a traditional semiconductor–metal interface, a difference in work function will result in bending of the bands of the semiconductor[18]. The work function of Pt is 5.7 eV, whereas the work function of carbon nanotubes is near 4.5 eV. Owing to this difference, a local polarization layer will develop on

the electrode–nanotube interface until the nanotube valence band edge aligns with the Fermi level of the metal electrode. Such pinning of the valence band edge to the Fermi level of the electrode was observed in scanning tunnelling spectroscopy experiments of semiconducting nanotubes on Au(111) (ref. 16). Away from the electrodes, the bands bend to lower energy (Fig. 1c, segment B). A gate voltage will not have a strong effect on the nanotube at position A and C owing to the screening of the nearby metallic leads and the capacitive coupling between the tube and the leads. In segment B, however, the electric field of the gate electrode will couple to the tube. For negative V_{gate} this will lead to an accumulation of holes and an increasing conductance, whereas for a positive V_{gate} the holes are depleted, yielding a lower conductance (Fig. 1c). Cooling the sample to 160 K, the metallic saturation resistance ($V_{gate} < -3$ V)

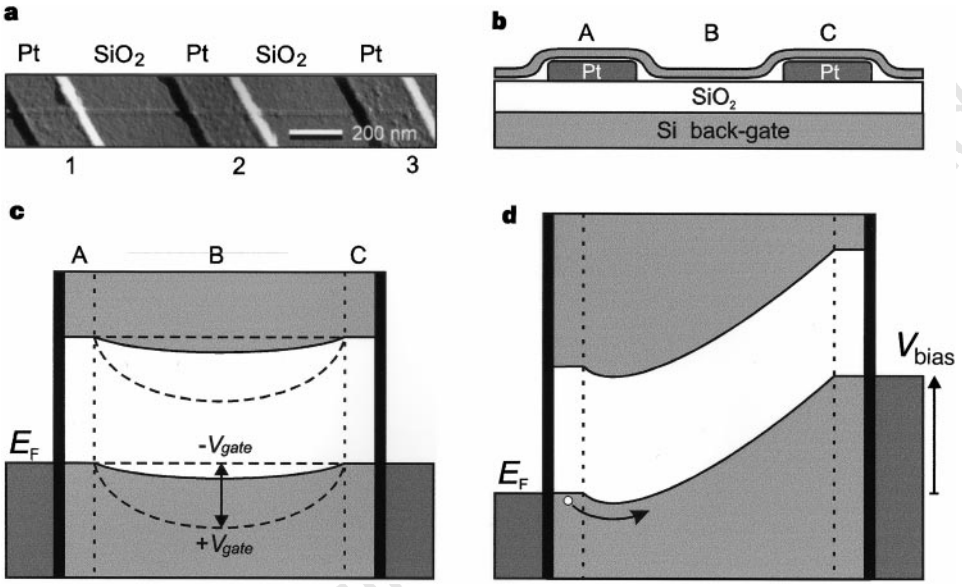

Figure 1 a, Tapping-mode AFM image of an individual carbon nanotube on top of three Pt electrodes. **b**, Schematic side view of the TUBEFET device. A single semiconducting nanotube is contacted by two electrodes. The Si substrate, which is covered by a layer of SiO_2 300 nm thick, acts as a back-gate. **c**, Suggested band diagram of the device. The nanotube with a gap of ~0.6 eV is connected to the leads with Fermi energy E_F by tunnelling contacts, indicated by the black vertical bars. At A and C (see **b**), the valence-band edge is pinned to the Fermi energy of the leads. Owing to a difference in work function between the tube and the electrodes, the bands bend towards lower energy in between the electrodes (B). For positive V_{gate} the bands bend more strongly, leading to an insulating state. For negative V_{gate} the bands flatten, resulting in a metal-like conductance. **d**, Application of a bias voltage results in a suppression of the barrier.

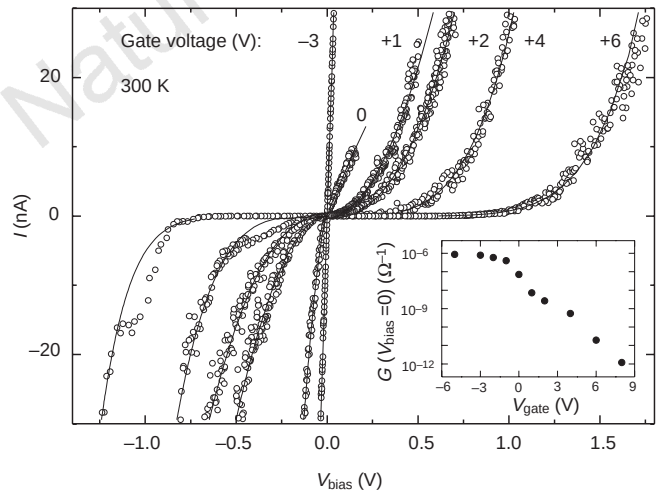

Figure 2 Two probe I–V_{bias} curves for various values of the gate voltage (V_{gate}). Data were taken at room temperature and in vacuum (~10^{-4} mbar), with the voltage applied to contacts 1 (drain) and 2 (source). A negative V_{gate} leads to ohmic behaviour while a positive V_{gate} results in a strong suppression of the current at low bias voltage and nonlinear I–V_{bias} curves at higher bias. Inset, conductance at $V_{bias} = 0$ as a function of V_{gate}. The conductance through this single molecular switch can be varied over at least six orders of magnitude and saturates at $10^{-6}\ \Omega^{-1}$ for negative V_{gate}.

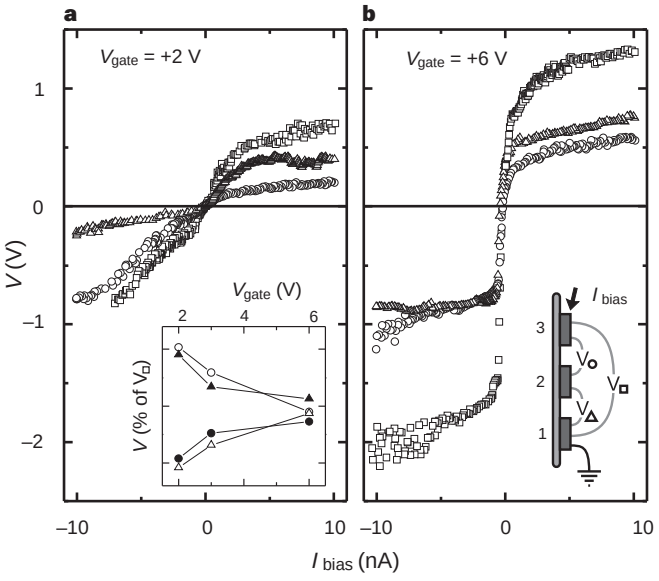

Figure 3 Three-probe I_{bias}–V curves for two gate voltages. The current is biased over the two outer contacts 1 and 3. The voltage drop is measured over contact pairs 1–2 (△), 2–3 (○) and 1–3 (□) (right inset). At low V_{gate} (**a**), the voltage drop over 1–2 is not the same as for 2–3, whereas for larger V_{gate} (**b**), the two voltages are identical. Left inset, voltages over pairs 1–2 and 2–3 as a percentage of the total voltage (1–3), both for negative bias (open symbols) and for positive bias (solid symbols). The observed behaviour is in agreement with the proposed band diagram of the device (Fig. 1).

increases from ~1 to ~4 MΩ. For a metallic tube we find the same room temperature resistance of ~1 MΩ and a similar dependence on temperature. This result supports the band diagram proposed above (Fig. 1c) because our model predicts that in segments A and C the tube should be metal-like owing to the pinning of the valence band edge. If, as an alternative model, there were an induced Schottky barrier[18] inside the tube at A and C, the device would exhibit a much stronger temperature dependence.

The suggested band structure of this device (Fig. 1c) is similar to that of a traditional semiconductor device, the so-called 'barrier injection transit time' (BARITT) diode[18]. This device consists of a semiconductor connected to two metal contacts, that is, two Schottky-type diodes connected back to back. Although we do not yet have a detailed understanding of the functioning of the TUBEFET, we shall attempt to give a qualitative description by using the well-known BARITT model. In both devices holes have to be transported over the barrier induced by the band bending (in segment B; Fig. 1c). When a bias is applied to a BARITT diode (Fig. 1d) an asymmetric space charge distribution results, because the barrier at the positive contact prevents holes from entering, whereas at the negative contact holes exit from the semiconductor, leaving a large space charge concentration. This leads to an asymmetry in electric field profile and correspondingly yields an unequal voltage drop over the right and left part of the device. When the electric field reaches through the entire device, current is able to flow.

We have performed current-bias transport measurements on the sample of Fig. 1a in a three-point configuration. We now can divide the sample into two segments: one between electrode pair 1–2 and one between pair 2–3. With the current source connected to electrode 3 and electrode 1 grounded, we can measure separately the voltage drops over these two tube segments. The total voltage over pair 1–3 is also measured, with electrode 2 left floating. The result for $V_{gate} = 2$ V is displayed in Fig. 3a. Again we observe gap-like features in the I–V curve. The voltages over the two segments indeed add up to the total voltage drop over the device. However, the voltage drop seems to be different for both segments, with most of the voltage dropping over segment 2–3 at negative bias. This is in agreement with the above described mechanism for a BARITT-like diode because at negative bias the potential of electrode 3 is lower than that of electrode 1, resulting in more space charge and thus a larger voltage drop near contact 3. For positive bias, electrode 1 has the lowest potential, yielding a larger voltage drop at electrode 1. This is indeed observed in the measurements. A different voltage division is observed when the same measurement is performed at a larger positive V_{gate} (Fig. 3b). The space-charge profile is now rather symmetric, as can be concluded from the almost equal voltage drop over segments 1-2 and 2-3. At large positive V_{gate}, more holes are depleted from the tube, leaving less room for an asymmetric space charge profile. With fewer free charges in the tube, it behaves more like an insulator and the dominant charge build-up is in the electrodes, resulting in equal voltage drops over the two segments. This trend is indicated in the inset of Fig. 3a, where the voltage over the two segments at −4 nA and +4 nA is plotted as a percentage of the total voltage (1–3) against V_{gate}.

Screening in truly one-dimensional conductors is expected to be different from that in a three-dimensional system. It is therefore of interest to deduce the typical length over which the bands are bent along the nanotube axis. From our data we can make a rough estimate of this value. Fig. 2 shows that at $V_{gate} = 0$ the tube is almost in the metallic state, and that the Fermi energy must therefore be close to the valence band edge throughout the device. If the band-bending length were short (≪400 nm), the Fermi level in the nanotube segments away from the electrodes would be located in the middle of the gap between conduction and valence band, and hole transport would be very hard because of the appreciable (~0.3 eV) barrier. If the band-bending length were very large (≫400 nm), however, no significant band bending would occur and the tube would respond similarly to a metallic tube. A negative gate voltage would thus have no effect. What we observe experimentally is something in between, and we thus conclude that, without applied electric fields, the band-bending length is roughly of the order of the distance between the electrodes, which is 400 nm.

The gain of the TUBEFET device can be estimated by considering the voltage over the device at a certain current. Going from +4 V to +6 V in V_{gate}, for example, results in a maximum change in voltage over the device of ~0.7 V (Fig. 2), which yields a gain of 0.35. The simplest way to improve this value in the current device geometry would be to decrease the SiO_2 layer thickness. Currently this is 300 nm but it could be reduced to ~5 nm (ref. 19), resulting in a gain of order 1 or higher. Other geometries that further increase the capacitance between the gate and the tube might also be possible. Considering the ultimate speed of the device, we calculate a ballistic traversal time of $\sim 10^{-13}$ s (or 10 THz) for 100 nm length of tube and a Fermi velocity for electrons in carbon nanotubes of 8×10^5 m s^{-1} (ref. 15). Another limitation to the device speed is the RC (resistance–capacitance) time. From Coulomb blockade measurements at low temperatures[5] we deduce that the total capacitance of a piece of nanotube 100 nm long in a similar device geometry is of order 10^{-18} F. With an 'on' resistance of 1 MΩ, this gives a frequency limit of 0.1 THz. At present the device resistance is dominated by the contact resistance[14]. If low-ohmic contacts can be realized, the two-probe resistance is expected to reach the lower quantum limit of about 6 kΩ, which would allow a maximum frequency of order 10 THz.

The fabrication of the TUBEFET, the single-molecule field-effect transistor described here, is relatively straightforward, and integration of multiple devices into a circuit may eventually be possible by using molecular self-assembly techniques[20]. Potential applications may therefore be possible, particularly as the device operates at room temperature and high switching speeds, and improved voltage gains seem possible.

In discussions of the fundamental limits of integrated circuit dimensions, warnings are often expressed that at some point radically new device structures should be used because of dominant quantum mechanical effects. Such new device concepts have been explored in the fields of mesoscopic physics and in molecular electronics. It is quite striking that it seems possible to describe qualitatively the ultra-small TUBEFET device, which is based on a single nanotube molecule, by the same semiclassical models that are used for devices in today's computer industry. □

Received 6 January; accepted 2 April 1998.

1. Aviram, A. & Ratner, M. A. Molecular rectifiers. *Chem. Phys. Lett.* **29,** 277–283 (1974).
2. Carter, F. L., Siatkowski, R. E. & Wohltjen, H. *Molecular Electronics Devices* (North Holland, Amsterdam, 1988).
3. Aviram, A. (ed.) *Molecular Electronics—Science and Technology* (AIP Conf. Proc. Vol. 262, 1992).
4. Joachim, C., Gimzewski, J. K., Schittler, R. R. & Chavy, C. Electronic transparence of a single C_{60} molecule. *Phys. Rev. Lett.* **74,** 2102–2105 (1995).
5. Tans, S. J. *et al.* Individual single-wall carbon nanotubes as quantum wires. *Nature* **386,** 474–477 (1997).
6. Porath, D. & Millo, O. Single electron tunneling and level spectroscopy of isolated C_{60} molecules. *J. Appl. Phys.* **81,** 2241–2244 (1997).
7. Reed, M. A., Zhou, C., Muller, C. J., Burgin, T. P. & Tour, J. M. Conductance of a molecular junction. *Science* **278,** 252–254 (1997).
8. Mintmire, J. W., Dunlap, B. I. & White, C. T. Are fullerene tubules metallic? *Phys. Rev. Lett.* **68,** 631–634 (1992).
9. Hamada, N., Sawada, A. & Oshiyama, A. New one-dimensional conductors: graphitic microtubules. *Phys. Rev. Lett.* **68,** 1579–1581 (1992).
10. Saito, R., Fujita, M., Dresselhaus, G. & Dresselhaus, M. S. Electronic structure of chiral graphene tubules. *Appl. Phys. Lett.* **60,** 2204–2206 (1992).
11. Iijima, S. & Ishihashi, T. Single-shell carbon nanotubes of 1-nm diameter. *Nature* **363,** 603–605 (1993).
12. Bethune, D. S. *et al.* Cobalt-catalysed growth of carbon nanotubes with single-atomic-layer walls. *Nature* **363,** 605–607 (1993).
13. Thess, A. *et al.* Crystalline ropes of metallic carbon nanotubes. *Science* **273,** 483–487 (1996).
14. Bezryadin, A., Verschueren, A. R. M., Tans, S. J. & Dekker, C. Multiprobe transport experiments on individual single-wall carbon nanotubes. *Phys. Rev. Lett.* **80,** 4036–4039 (1998).
15. Dresselhaus, M. S., Dresselhaus, G. & Eklund, P. C. *Science of Fullerenes and Carbon Nanotubes* (Academic, San Diego, 1996).

16. Wildoer, J., Venema, L. C., Rinzler, A. G., Smalley, R. E. & Dekker, C. Electronic structure of atomically resolved carbon nanotubes. *Nature* **391,** 59–62 (1998).
17. Odom, T. W. *et al.* Atomic structure and electronic properties of single-walled carbon nanotubes. *Nature* **391,** 62–64 (1998).
18. Sze, S. M. *Semiconductor Devices—Physics and Technology* (Wiley, Toronto, 1985).
19. Hirose, H., Hiroshima, M., Yasaka, T., Takakura, M. & Miyazaki, S. Ultra-thin gate oxide growth on hydrogen terminated silicon surfaces. *Microelectron. Eng.* **22,** 3–10 (1993).
20. Ullman, A. *An Introduction to Ultrathin Organic Films* (Academic, San Diego, 1991).

Acknowledgements. We thank R. E. Smalley and co-workers for the supply of the indispensable single-wall carbon nanotubes; A. Bezryadin, C.J.P.M. Harmans and P. Hadley for discussions; A. van den Enden for technical assistance. The work was supported by the Dutch Foundation for Fundamental Research on Matter (FOM).

Correspondence and requests for materials should be addressed to C.D. (dekker@qt.tn.tudelft.nl).

Organic-functionalized molecular sieves as shape-selective catalysts

Christopher W. Jones, Katsuyuki Tsuji & Mark E. Davis

Chemical Engineering, California Institute of Technology, Pasadena, California 91125, USA

Zeolites and related crystalline molecular sieves can possess catalytically active acid sites, as well as uniformly sized and shaped pores and voids, that allow for their industrial use as shape-selective catalysts[1]. Some catalytic reactions that are not mediated by acids (such as oxidation) have also been shown to occur in zeolites in a shape-selective manner[2], but the diversity in active sites in these materials remains restricted. For mesoporous materials[3], the diversity in catalytic activity has been broadened by grafting organosilanes that contain organic functional groups onto the internal pore surfaces[4–6] or by incorporating them into the structure during the synthesis process[7–12]. The former approach has not proven straightforward for microporous zeolites because a large fraction of the grafted functional groups become attached instead to the exterior surfaces of the crystal, where there is no shape selectivity[13]. The synthesis of zeolites and molecular sieves using organosilanes as structure-directing agents has been accomplished[14,15], but the subsequent creation of porosity requires the complete loss of the organic functional groups. Here we report a new methodology that overcomes these problems and allows the production of microporous molecular sieves containing organic functionalities within their pores. During the initial synthesis phase, phenethyl groups covalently tethered to silicon atoms are incorporated into the framework. The external surface-bound functionalities and the structure-directing agents residing within the intracrystalline spaces are then removed to create a microporous material. Subsequent sulphonation of the phenyl rings produces intrapore sulphonic acid sites that perform shape-selective catalysis. Different active-site types can be created by attaching other functional groups to the framework silicon, and we therefore expect that our method will lead to the formation of a wide range of shape-selective catalysts.

A major key to success in synthesizing organic-functionalized molecular sieves (OFMSs) is the identification of a molecular sieve that can be prepared in the absence of an organic structure-directing agent (SDA) such as NaY, or where the SDA can be removed by extraction. We have synthesized OFMs by both routes, for example NaY (no organic SDA) or pure-silica zeolite beta using tetraethylammonium fluoride (TEAF) as the SDA. We prefer the use of high-silica materials because they provide a hydrophobic void space in which to conduct chemical reactions. An example of the synthetic methodology is illustrated by the synthesis of pure-silica zeolite beta using TEAF as the SDA in the presence of phenethyltrimethoxy silane (PETMS). Following the procedure of Camblor *et al.*[16] for the synthesis of pure-silica zeolite beta using TEAF as the SDA, we crystallized the hybrid material with 5 atom% or less (2.8 atom% for the sample described here) of the silicon substituted by PETMS. The X-ray diffraction pattern of the hybrid material clearly identifies it as crystalline zeolite beta (diffraction pattern available: see Supplementary information). Figure 1 shows the ^{29}Si cross-polarization magic angle spinning (CPMAS) NMR spectra for the as-synthesized, pure-silica zeolite beta and the organic-functionalized beta. It is clear from the spectrum of the hybrid material that the phenethyl group (the presence of the aromatic ring was verified by Raman spectroscopy, spectra available, see Supplementary information) is covalently linked to the framework silicon atom (peak at −68 p.p.m.: C–Si–$(OSi)_3$; refs 14, 17). This resonance indicates that the linking silicon atom is fully condensed in the framework[18].

Organic functionalities on the exterior surface of the beta crystals can be removed by reacting the as-synthesized material with concentrated sodium hydroxide solutions (~8 M NaOH, 5% methanol, 25 °C, 1 h). Subsequently, extraction of TEAF from the hybrid material is possible by repeated exposures to acetic acid/water mixtures at 140 °C. Essentially complete removal of TEAF is accomplished for the sample described here (>99% removed as determined by thermogravimetric analysis). The extracted OFMS is sulphonated by contact with vapour from 30% SO_3/H_2SO_4 at room temperature after heating at ~100 °C under a vacuum of less than 10^{-6} torr overnight. Following sulphonation, the sample is washed with water and then dioxane to remove residual sulphuric acid resulting from the sulphonation procedure. Scanning electron microscopy (SEM) images of this fully modified material do not appear different from the images of the as-made material. Before use as a catalyst, the solid is dehydrated at ~100 °C for at least 6 h under a vacuum of less than 10^{-6} torr. Verification of sulphonic acid formation is obtained by Raman spectroscopy (spectrum available, see Supplementary information). Nitrogen adsorption isotherms indicated that the extraction procedure creates significant microporosity (isotherm available, see Supplementary information). Figure 2 illustrates this synthetic procedure.

The reaction of a cyclic ketone with ethylene glycol is used to illustrate the catalytic activity and shape-selectivity of the sulphonated, extracted phenyl-functionalized beta (beta/PETMS/SO_3H). The beta/PETMS/SO_3H is an active catalyst for the formation of 2,2-pentamethylene-1,3-dioxolane (cyclic ketal) from ethylene glycol and cyclohexanone (HEX). This activity is due to the phenyl-sulphonic acid groups covalently linked to the zeolite framework. The data in Table 1 show that *para*-toluenesulphonic acid monohydrate, phenyl-sulphonic acid anchored to controlled-pore-glass (CPG-240, mean pore diameter 240 Å), and beta/PETMS/SO_3H are active catalysts for this transformation. None of the OFMS synthesis intermediates and the non-functionalized, pure-silica materials are

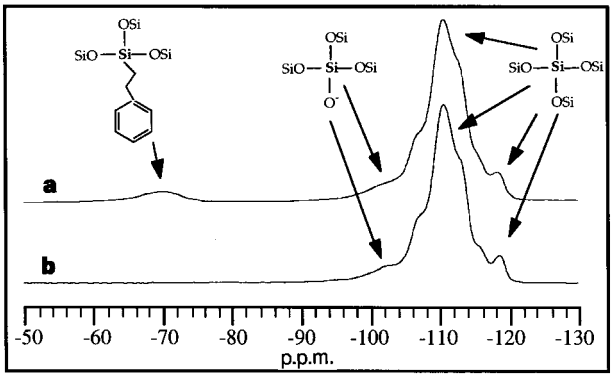

Figure 1 ^{29}Si CPMAS NMR spectra of **a**, organic-functionalized beta and **b**, pure-silica beta. Spectra are from as-synthesized materials and are referenced to tetramethylsilane.